



# Decoupling Mass Transport and Electron Transfer by a Double-Cathode Structure of Li-O<sub>2</sub> Battery with High Cyclic Stability

Qing Han,<sup>1,4</sup> Wei Guo,<sup>1,4</sup> XiaoFeng He,<sup>1</sup> TongChao Liu,<sup>2</sup> Xiao Liu,<sup>1</sup> Xuebing Zhu,<sup>1</sup> Tengfei Bian,<sup>1</sup> Lei Jiang,<sup>3</sup> Jun Lu,<sup>2,\*</sup> and Yong Zhao<sup>1,\*</sup>

<sup>1</sup>Key Lab for Special Functional Materials of Ministry of Education; National & Local Joint Engineering Research Center for High-efficiency Display and Lighting Technology; School of Materials Science and Engineering; Collaborative Innovation Center of Nano Functional Materials and Applications; Henan University, Kaifeng, 475004, P. R. China

<sup>2</sup>Chemical Sciences and Engineering Division, Argonne National Laboratory, Lemont, Illinois 60439, USA

<sup>3</sup>Key Laboratory of Bio-inspired Materials and Interfacial Science, Technical Institute of Physics and Chemistry, Chinese Academy of Sciences, Beijing, 100190, P. R. China

<sup>4</sup>These authors contribute equally to the work.

\* Correspondence: zhaoyong@henu.edu.cn

\* Correspondence: junlu@anl.gov

## SUMMARY

Aprotic lithium-oxygen (Li-O<sub>2</sub>) batteries have attracted extensive attention due to their ultrahigh theoretical energy density. However, slow and undesired electron transfer during cathodic reactions causes low cyclic stability in these batteries. Herein, we demonstrate that O<sub>2</sub> mass transport and electron transfer for cathodic reactions in Li-O<sub>2</sub> batteries could be decoupled by a double-cathode structure that efficiently enables stable electron transfer between cathode and Li<sub>2</sub>O<sub>2</sub>/O<sub>2</sub>. This resolves various side reactions and slow Li<sub>2</sub>O<sub>2</sub> reaction kinetics issues in conventional Li-O<sub>2</sub> batteries, leading to stable operation of the cell nearly 2 months at a capacity of 0.1 mAh cm<sup>-2</sup> and at a capacity of 5 mAh cm<sup>-2</sup>, respectively, a more than 4-fold and 10-fold increases in cycle life when compared to single-cathode batteries. These remarkable improvements in the cyclic stability of Li-O<sub>2</sub> batteries with double cathodes provides an interesting concept for improving the operational stability of other metal rechargeable batteries with conversion-type chemistry.

electron transfer pathway, lithium oxygen battery, redox mediator, cycle life, double-cathode structure, stable and continuous electron transfer, mass transport, side reactions, cathode passivation, barrier layer

## INTRODUCTION

Aprotic lithium-oxygen (Li-O<sub>2</sub>) batteries with ultrahigh theoretical energy density (~3500 Wh kg<sup>-1</sup>) have attracted much attention as next-generation batteries.<sup>1-8</sup> The typical structure of these batteries consists of a lithium anode, a porous cathode, and a separator wetted with a non-aqueous electrolyte.<sup>9</sup> During discharge reaction processes, O<sub>2</sub> is reduced into Li<sub>2</sub>O<sub>2</sub> with lithium ions by accepting electrons from the cathode (2Li<sup>+</sup>+O<sub>2</sub>+2e<sup>-</sup>→Li<sub>2</sub>O<sub>2</sub>)<sup>10</sup>. However, the discharged Li<sub>2</sub>O<sub>2</sub> product has low electrical conductivity and nonhomogeneous coverage on the cathode that could result in the slow electron transfer between the cathode and O<sub>2</sub>,<sup>11-15</sup> finally oxygen reduction reaction (ORR) is terminated.<sup>16</sup> Moreover, the slow electron transfer between the cathode and Li<sub>2</sub>O<sub>2</sub> limits oxygen evolution reaction kinetics (OER, Li<sub>2</sub>O<sub>2</sub>→2Li<sup>+</sup>+O<sub>2</sub>+2e<sup>-</sup>) and increases the charge potential (>4.0 V) during cycling. High charge potential not only promotes the production of numerous reactive <sup>1</sup>O<sub>2</sub> and related side reactions, but also triggers oxidative degradation of the electrolyte and cathode.<sup>17</sup> Therefore, the slow electron transfer between cathode and Li<sub>2</sub>O<sub>2</sub>/O<sub>2</sub> during ORR and OER is the most notable challenge causing short cycle lives that consequently restrict the fundamental development and practical application of Li-O<sub>2</sub> batteries.<sup>18-20</sup>

Different strategies developed in efforts to solve these problems include constructing functional electrode materials<sup>21-27</sup>, regulating electrolyte components,<sup>28-32</sup> that could promote

## Context & Scale

Aprotic lithium-oxygen (Li-O<sub>2</sub>) batteries have attracted extensive attention due to their ultrahigh theoretical energy density. However, slow and undesired electron transfer during cathodic reactions causes low cyclic stability during cathodic reactions in these batteries. Herein, we demonstrate that O<sub>2</sub> mass transport and electron transfer for cathodic reactions in Li-O<sub>2</sub> batteries could be decoupled by a double-cathode structure that efficiently enables stable electron transfer between cathode and Li<sub>2</sub>O<sub>2</sub>/O<sub>2</sub>. This resolves various side reactions and slow Li<sub>2</sub>O<sub>2</sub> reaction kinetics issues in conventional Li-O<sub>2</sub> batteries, leading to stable operation of the cell nearly 2 months at a capacity of 0.1 mAh cm<sup>-2</sup> and at a capacity of 5 mAh cm<sup>-2</sup>, respectively, a more than 4-fold and 10-fold increases in cycle life when compared to single-cathode batteries. These remarkable improvements in the cyclic stability of Li-O<sub>2</sub> batteries with double cathodes provides an interesting concept for improving the operational stability of other metal rechargeable batteries with conversion-type chemistry.



the electron transfer between cathode and  $O_2/Li_2O_2$  to extend the battery cycle life. For example, solid catalysts have been developed to accelerate  $Li_2O_2$  reaction kinetics.<sup>33-36</sup> However, limited by the small contact area between the solid catalyst and  $Li_2O_2$ , it is difficult to enable stable electron transfer pathways for ORR and OER at the cathode.<sup>20,37,38</sup> Furthermore, the catalytic selectivity of most solid catalysts is relatively poor, leading to undesired side reactions between the cathode and electrolyte.<sup>20,39,40</sup> In this sense, supplementing soluble redox mediator (RM) catalysts as electron carriers into the electrolyte has been proposed to achieve fast electron transfer between the cathode and  $O_2/Li_2O_2$ .<sup>41-46</sup> For instance, 2,5-di-tert-butyl-1,4-benzoquinone (DBBQ) and 2,2,6,6-tetramethyl-1-piperidinyloxy (TEMPO) are potential candidates utilized as ORR and OER RM catalysts, respectively.<sup>9,41</sup> In principle, soluble RMs improve the energy efficiency of the battery thanks to the stable electron transfer among  $O_2/Li_2O_2$ , RMs and cathode. They also simultaneously suppress the production of reactive oxygen intermediates, such as superoxide radical ( $O_2^{\cdot-}$ ) and singlet oxygen ( $^1O_2$ ), thus reducing the chemical degradation of battery components and enhancing the battery stability.<sup>41</sup> However,  $Li-O_2$  batteries assembled with hybrid OER and ORR RM catalysts still fall short to achieve long-term cycle life. The underline reason is that, during battery operation, the continuous accumulation of  $Li_2O_2$  through  $O_2$  reduction and byproducts on the cathode passivates its surface, typically in the late stage of cell operation or large capacities,<sup>18,47</sup> blocking electron transfer between the cathode and RMs. Therefore, the RM catalysts cannot effectively and continuously exchange electrons with the cathode, resulting in an inevitable increase in the charge overpotential. The high charging potential in turn triggers undesired electron transfer between the cathode and electrolyte, resulting in severe side reactions, especially the degradation of RM catalysts. Hence, maintaining stable and continuous electron transfer among the cathode, RM catalysts, and  $Li_2O_2/O_2$  is critical for achieving long cycle life and high energy efficiency in  $Li-O_2$  batteries. Unfortunately, this battery chemistry and the associated electron transfer pathways have yet to be established.

In this work, we demonstrate a proof-of-concept that the  $O_2$  mass transport and electron transfer for cathodic reactions ( $2Li^+ + O_2 + 2e^- \leftrightarrow Li_2O_2$ ) can be decoupled in a double-cathode structured electrode design, where the cell consists of a lithium anode, a separator, an electrolyte with RM catalysts (DBBQ and TEMPO), an inner cathode, an  $O_2$  barrier layer and an outer cathode (Figure 1). The functions of the  $O_2$  barrier layer are to prevent  $O_2$  mass transport to the inner cathode, and the solution-mediated ORR process and  $Li_2O_2$  nucleation/storage can be realized at the outer cathode. Simultaneously, the inner cathode can realize stable electron transfer with RM catalysts. Such a structure ensures stable and continuous electron transfer between the cathode, RM catalysts, and  $Li_2O_2/O_2$  during battery cycling, which provides a continuous driving force for  $Li_2O_2$  reactions at low overpotentials, thereby preventing side reactions. Remarkably, it achieves a more than 4-fold and 10-fold increases in cycle life at the capacities of 0.1 and 5 mAh  $cm^{-2}$ , respectively, when compared to single-cathode batteries, enabling stable operation to approximately 2 months, a record-high value among the existing  $Li-O_2$  batteries containing RM catalysts. This work opens a door for the fundamental development and practical use of aprotic  $Li-O_2$  and  $Li$ -air batteries and has key value for upgrading the operational stability of other metal rechargeable batteries with conversion-type chemistry, such as  $Li-CO_2$  and  $Li$ -organic positive electrodes.

## RESULTS

### The working principle of aprotic $Li-O_2$ battery

Figure 1A shows a conventional  $Li-O_2$  battery (denoted as **Type A**), which is composed of a lithium anode, a separator with an electrolyte and a porous cathode. During cell operating, the high charge voltage caused by slow electron transfer between  $Li_2O_2$  and cathode usually induces side reactions involving the electrolyte and carbon electrode, resulting in the accumulation of by-products on the cathode (Figure S1A). Therefore, the cycle life of this type cell design is limited. In response to these problems, soluble OER and ORR RM catalysts are introduced into the  $Li-O_2$  battery as electron transfer carriers (denoted as **Type B**, Figure 1B). RM catalysts can promote electron transfer between  $Li_2O_2$  and the cathode in the solution phase, which substantially inhibits electrolyte degradation and reduces by-product formations. However, due to cathode passivation caused by the gradual accumulation of product and byproduct after long-term cycling, RM catalysts cannot be effectively reduced/oxidized by the cathode. The charge voltage continues to increase, leading to intensified side reactions and battery instability in a long-term run (Figure S1B). We, therefore, construct a double-cathode structured  $Li-O_2$  battery (denoted as **Type C**, Figure 1C), featuring an inner cathode and an outer cathode with an  $O_2$  barrier layer in between with a hope to solve mass transport and electron transfer simultaneously. The inner cathode in this cell design provides a new and stable electron transfer channel for the reduction/oxidation of RM catalysts. When the outer cathode is passivated due to the coverage of discharge product  $Li_2O_2$  and/or byproduct, the inner cathode can continuously exchange electrons with RM



catalysts, and the activated RM catalysts immediately migrate to the outer cathode to promote solution-mediated nucleation/storage and decomposition of  $\text{Li}_2\text{O}_2$ . Importantly, to prevent the inner cathode from being covered by  $\text{Li}_2\text{O}_2$ , an  $\text{O}_2$  barrier layer is placed between the two cathodes. This layer acts as a membrane to block the  $\text{O}_2$  mass transport to the inner cathode (Figures S1C and S1D). The combination of barrier layers and inner cathode realizes the decoupling of  $\text{O}_2$  mass transport and electron transfer at the cathode part of double-cathode structured Li- $\text{O}_2$  cell, which enables stable and continuous electron transfer among cathode, RM catalysts, and  $\text{Li}_2\text{O}_2/\text{O}_2$ , and maintains low overpotential during long cycling test.

### The performance of Li- $\text{O}_2$ cells

First, we assembled the three types of batteries, as shown in Figures 1A-1C, and the most representative DBBQ and TEMPO molecules were selected as the ORR and OER redox catalysts. An artificial membrane close to the anode is applied to inhibit the diffusion of RM catalysts (if used) to lithium anode (see the Figure S2 and Note S1). To eliminate the influence of the inner cathode on the battery performance, the cathodes of Type A and B cells are the superposition of two carbon electrodes (the inner and outer parts of a single cathode are referred to as SC-IC and SC-OC, respectively, Figure S2A and S2C). In contrast, the cathode in Type C is composed of inner and outer cathodes separated by an  $\text{O}_2$  barrier layer (the inner and outer parts of double cathodes are referred to as DC-IC and DC-OC, respectively, Figure S2B and S2D). Polypropylene film is selected as the barrier layer owing to its low surface porosity (percentage of the pore area per unit area, ~15%), pore size (~250 nm) and suitable thickness (~10  $\mu\text{m}$ ), more detailed information as shown in Table S3. Galvanostatic discharge-charge tests were first performed with these three types of cells. As shown in Figure 1D, Type B cells exhibit lower charging potentials and higher capacities than Type A (without RM catalysts). Clearly, the RM catalysts promotes  $\text{Li}_2\text{O}_2$  reaction kinetics, which has been well documented previously.<sup>9,41</sup> Notably, the Type C battery also shows a lower overpotential with over three-fold increase in capacity when compared to Type B (Figure S3A). In addition, the rate capability of Type C cell at the current densities of 0.1–1  $\text{mA cm}^{-2}$  are also much better than that of Type B with single cathode (Figure S3B). From the cyclic voltammetry curves of Type B and C cells, the redox peak currents from RM catalysts are similar (Figure S4). This verifies that the difference in the cathode structure does not affect the original redox properties of RM catalysts.

The cycle performance and overpotential of the Type C cell with a capacity of 0.1  $\text{mAh cm}^{-2}$  were further evaluated. Figure 1E shows that the charge voltage of Type C cell in the initial 120 cycles are stable and well below 3.8 V, while the charge voltages of Type B and A cells increase to 4.0 V and 4.5 V after 90 cycles, respectively. This illustrates that Type C battery with double cathodes exhibit a voltage plateau and  $\text{Li}_2\text{O}_2$  reaction kinetics superior to those of Type A and B. More importantly, the cycle life of Type C are approximately 3 and 6 times that of Type B and A cells, respectively, achieving 1100 cycle numbers (approximately 2 months) at a capacity of 0.1  $\text{mAh cm}^{-2}$  (Figure 1F). To further confirm our concept, we tested the cycle stability in the case of a higher areal capacity on Type B and C batteries. At a capacity of 5  $\text{mAh cm}^{-2}$  (Figures 1G and 1H), the Type B battery cannot completely discharge in the second cycle, and the Type C battery can still cycle stably at a lower overvoltage. As a result, the double-cathode Type C battery shows excellent cycle life over 1100 h, which is much higher than those of single-cathode Type B battery (Figure S5). Clearly, it is feasible to enhance cell cycle life with the double-cathode structure design.

### Analysis of the battery performance difference

To explore the enormous difference in cell performance between Type B and C batteries, we monitor the morphologies of discharge products on the two cathodes with the same capacities (5  $\text{mAh cm}^{-2}$ ) by scanning electron microscopy (SEM). Pristine outer cathode and inner cathode have shown in Figure S6. Figure 2A shows a large number of discharge products deposited on both inner and outer of the cathode in the Type B cell (with single cathode). In contrast, many discharge products can also be found in the outer cathode in the Type C cell, but the inner cathode remains relatively clean (Figure 2B). We note that the double-cathode structure design (Type C) promotes the solution-mediated ORR and  $\text{Li}_2\text{O}_2$  nucleation/storage on the outer cathode. The X-ray diffraction (XRD) pattern reveals the discharge products on the cathode to be  $\text{Li}_2\text{O}_2$ <sup>43,48</sup> and can be reversibly decomposed after recharging (Figures 2C and S7). The difference between Type B and C batteries is the absence and presence of an  $\text{O}_2$  barrier layer between the two cathodes. Then we observed the  $\text{Li}_2\text{O}_2$  deposition on  $\text{O}_2$  barrier layer, as indicated in Figure S8. The SEM shows that the side of barrier layer near the outer cathode deposit a large amount of  $\text{Li}_2\text{O}_2$ , while the side near the inner cathode deposited less. This result indicate that the  $\text{O}_2$  barrier layer can effectively prevent the  $\text{O}_2$  mass transport to the inner cathode region. After recharging, the  $\text{Li}_2\text{O}_2$  on the  $\text{O}_2$  barrier layer disappears,



indicating that the formation and decomposition of  $\text{Li}_2\text{O}_2$  in the double-cathode Type C battery is reversible.

To further confirm the influence of the  $\text{O}_2$  barrier layer on the storage of  $\text{Li}_2\text{O}_2$ , the quantity of  $\text{Li}_2\text{O}_2$  deposited on the inner and outer cathodes of the two type of cells is quantitatively analyzed by iodometric titration experiments. Figure 2D shows that approximately 48% and 52% of  $\text{Li}_2\text{O}_2$  are detected on the inner and outer cathodes, respectively, in the Type B cell. In sharp contrast, only 19% of  $\text{Li}_2\text{O}_2$  is deposited on the inner cathode, and most of the  $\text{Li}_2\text{O}_2$  (approximately 81%) is deposited on the outer cathode and on the  $\text{O}_2$  barrier layer in the Type C cell. These results demonstrate that the existence of an  $\text{O}_2$  barrier layer can greatly block  $\text{O}_2$  mass transport to the inner cathode, preventing the discharge product  $\text{Li}_2\text{O}_2$  from depositing on the inner cathode; thereby, the electron transport between the RM catalysts and the inner cathode can proceed stably and efficiently. Therefore, the  $\text{O}_2$  barrier layer is the key factor to decouple the electron transfer on the inner cathode and  $\text{Li}_2\text{O}_2$  nucleation/ storage on the outer cathode.

To study the effect of the barrier layer on  $\text{O}_2$  mass transport and deposition process of  $\text{Li}_2\text{O}_2$  on the cathode, we used COMSOL software to simulate the quantities of transported  $\text{O}_2$ , diffused RMs, and deposited  $\text{Li}_2\text{O}_2$  during the discharge process of Type B and C cells.<sup>49</sup> Figures 3A and 3B are the models of the cathode structure in Type B and C batteries, which are used to simulate the changes in the quantity of chemical substances ( $\text{O}_2$ ,  $\text{Li}_2\text{O}_2$  and RMs) inside the battery (see the ESI† and Table S3 for detailed information on the simulation data). Herein, the Type B cell consists of superposed outer and inner cathodes, and the Type C cell consists of an outer cathode, an  $\text{O}_2$  barrier layer and an inner cathode. In both Type B and C cells, the initially saturated concentration of  $\text{O}_2$  in the electrolyte is approximately 3.8 mM, and the inner and outer cathodes are flooded with electrolyte (50 mM DBBQ and 200 mM TEMPO) to reflect the real operating condition of the cell.

Figures 3C-3H shows the simulated  $\text{O}_2$ , DBBQLi and  $\text{Li}_2\text{O}_2$  concentrations of Type B and Type C cells. In the Type B cell,  $\text{O}_2$  is consumed to generate  $\text{Li}_2\text{O}_2$  on the cathode when the discharge starts. Meanwhile, a concentration gradient of  $\text{O}_2$  is established from the outer cathode near the electrolyte/gas interface to the inner cathode (Figure 3C). After discharging to 1000 s, the concentrations of  $\text{O}_2$ , DBBQ and DBBQLi reach a steady state and remain constant (Figure S9). However, there is still about 0.7 mM  $\text{O}_2$  at the deepest inner cathode region (240  $\mu\text{m}$ ), indicating that  $\text{O}_2$  mass transport rate can keep up with the discharge current. Excess  $\text{O}_2$  is immediately reduced in the cathode region when it meets DBBQLi, thus the ORR will continue to occur in the inner cathode region. The simulation result in Figure 3G shows that the discharge product  $\text{Li}_2\text{O}_2$  distributed on the inner cathode and outer cathode are comparatively even, which is consistent with the SEM observation and  $\text{Li}_2\text{O}_2$  iodometric titration experiments in Figure 2.

In the Type C cell, the simulation results show that  $\text{Li}_2\text{O}_2$  mainly forms in the outer cathode, and only a small amount in the inner cathode (Figure 3H). At the beginning of the discharge, the dissolved  $\text{O}_2$  in the inner cathode region form a small amount of discharge products. Since the  $\text{O}_2$  barrier layer has a significant effect on preventing  $\text{O}_2$  transport to the inner cathode, the  $\text{O}_2$  concentration gradient between the inner and outer cathode becomes higher and higher as the ORR reaction progresses (Figure 3D). When discharging reaches 680 s, the  $\text{O}_2$  concentration in the inner cathode region is close to 0 mM, thereby the ORR reaction mainly occurs in the outer cathode region after 680 s.

The  $\text{O}_2$  barrier layer prevents the deposition of discharge product on the inner cathode at a large extent. The relatively clean inner cathode ensures efficient electron transfer from/to RM catalysts. Nevertheless, the  $\text{O}_2$  barrier layer has no selectivity for  $\text{O}_2$  and the oxidized or reduced RMs. Similar to the  $\text{O}_2$  diffusion in Figure 3D, the barrier layer is also resistant to DBBQLi diffusion (Figure 3F). However, it is worth noting that there is still about 7 mM of DBBQLi that can pass through the barrier layer to maintain stable electron transfer when discharging to 1000 s (Figure S10). Such positive results attribute to higher concentration of RMs (50 mM DBBQ and 200 mM TEMPO is much larger than the 3.8 mM  $\text{O}_2$ ). A higher concentration of DBBQLi accumulates in the inner cathode during battery operation, and this high concentration gradient can provide a strong driving force for the diffusion of DBBQLi. Therefore, enough DBBQLi can penetrate the  $\text{O}_2$  barrier layer, thereby ensuring that a sufficient quantity of DBBQLi on the outer cathode participates in the chemical reduction reaction of  $\text{O}_2$ .

To further verify the results of the experiment, we used H-type cells to conduct a simple penetration experiment on  $\text{O}_2$  and DBBQ (Figures S11 and S12). The results show that the  $\text{O}_2$  barrier layer can effectively prevent  $\text{O}_2$  transport from left to right. After 12 hours, the  $\text{O}_2$  concentration in the right chamber was only 0.9 mg/L, much lower than that in the left chamber (~8.1 mg/L) (Table S1). This confirms the blocking effect the  $\text{O}_2$  barrier layer (surface porosity of 15%, denoted as SP 15%) in the Type C cell inhibiting  $\text{O}_2$  transport to the inner cathode. For the DBBQ penetration experiment (Figure S12), the DBBQ concentration



in the left chamber was 50 mM. After 12 hours, the solution in the right bottle turned yellowish, indicating that DBBQ can penetrate through the O<sub>2</sub> barrier layer. Quantitative analysis (Figures S13 and Table S2) showed that the concentration of DBBQ was 10.9 mM. Such concentration difference indicates that the quantities of RM catalysts are more than sufficient to reduce O<sub>2</sub> and decompose Li<sub>2</sub>O<sub>2</sub> under these conditions.

To simulate the true state of the battery during operation, we further simulated the subsequent Li<sub>2</sub>O<sub>2</sub> accumulation when the outer cathode was passivated to different levels in Type C cells (Figure S14). The results show that the subsequent Li<sub>2</sub>O<sub>2</sub> still deposits on the outer cathode under different passivation levels, which further proves the stable and continuous electron transfer with the double-cathode structure. In conclusion, the simulation results illustrate that the double-cathode Type C battery changes O<sub>2</sub> mass transport and electron transfer during cell cycling, especially at the late stage of cell operation and large capacities, thereby fully guarantees efficient electron transfer between RM catalysts and inner cathode.

### Side reactions in Type B and C cells

The above research results clarify that the double-cathode structure can decouple O<sub>2</sub> mass transport and electron transfer with the O<sub>2</sub> barrier layer and inner cathode, leading to stable and effective electron transfer between the cathode, RM catalysts, and Li<sub>2</sub>O<sub>2</sub>/O<sub>2</sub>. To further evaluate the efficacy of double-cathode structure cells in enabling efficient electron transfer, we used differential electrochemical mass spectrometry (DEMS) to analyze the quantity of O<sub>2</sub> consumption and production during discharge and charge. In Figure 4A, Type B cell has lower discharge potentials, with a 2e<sup>-</sup>/O<sub>2</sub> rate of 1.09 during the discharge process. It indicates that undesired electron transfer occurs between the cathode and electrolyte, which can be ascribed to side reaction induced by oxygen intermediates (Scheme 1A).<sup>43,50,51</sup> In contrast, the discharge potentials of a double-cathode Type C cell are stable, and the 2e<sup>-</sup>/O<sub>2</sub> rate is closer to 1 (1.02), indicating that the double-cathode structure can promote stable and effective electron transfer and avoid side reactions (Figures 4C and Scheme 1B).

During cell recharge, the Type B cell exhibits higher charging potentials with a ratio of 2e<sup>-</sup>/O<sub>2</sub> to be 1.08 (Figure 4B), showing that significant side reactions occur on the cathode side during the decomposition of Li<sub>2</sub>O<sub>2</sub>. The RM catalyst cannot be effectively activated due to limited electron exchange with the passivated cathode, resulting in an increase in the charge voltage, which triggers a series of side reactions (Scheme 1A). The charging curves of the Type C cell are relatively stable with a 2e<sup>-</sup>/O<sub>2</sub> rate close to 1 (1.01), indicating that there are minimum side reactions in Type C cell (Figure 4D). When the outer cathode cannot stably and continuously transfer electrons owing to Li<sub>2</sub>O<sub>2</sub> coverage, the clean inner cathode accepts electrons from the RM catalysts, which reduces the charging potentials (Scheme 1B). The extremely low 2e<sup>-</sup>/O<sub>2</sub> rate is due to the double-cathode structure, which decouples Li<sub>2</sub>O<sub>2</sub> nucleation/storage and electron transfer at space scale, makes electron transfer fluid among the RM catalysts, cathode, and O<sub>2</sub>/Li<sub>2</sub>O<sub>2</sub>, and enhances Li<sub>2</sub>O<sub>2</sub> reaction kinetics. As a result, side reaction due to undesired electron transfer is inhibited.

To further confirm the positive benefits of using double-cathode structures to inhibit side reactions, we characterized inner and outer cathode morphologies for Type B and C cells after 170 cycles. Figures 5A and 5D show the original morphology of the outer and inner cathodes, respectively. After cycling, a thick passivation layer on the carbon electrode surface in Type B cell can be clearly observed (Figures 5B and 5E). The existence of a passivation layer makes it difficult to realize the stable and continuous electron transfer process between the cathode and RM catalysts, resulting in early cell failure. For the Type C cell, the inner and outer cathodes are still smooth and clean after 170 cycles (Figures 5C and 5F). This is because the inner cathode can continuously activate the RM catalysts to promote the nucleation/storage and decomposition of Li<sub>2</sub>O<sub>2</sub> on the outer cathode, thereby reducing charging potentials and associated side reactions. We then further analyzed compositions at the electrode surface by Raman spectroscopy. After the same number of cycles, undecomposed Li<sub>2</sub>O<sub>2</sub> and typical by-products, such as CH<sub>3</sub>COOLi and Li<sub>2</sub>CO<sub>3</sub>, were detected on both the inner and outer cathodes of Type B cell (Figure 5G). In contrast, no product/by-product peaks were detected on the inner and outer cathodes in Type C cell. In addition, we also analyzed the inner and outer cathodes in the case of high areal capacity (5 mAh cm<sup>-2</sup>). The SEM results show that a large amount of undecomposed product and by-product accumulate on the inner and outer cathodes in the single-cathode battery (Figure S15). In contrast, the cathode of the double-cathode battery is relatively clean. The situation is similar as those of Li-O<sub>2</sub> batteries cycling at low capacity (0.2 mAh cm<sup>-2</sup>) after 170 cycles. Whether in long-term cycle or large-capacity cycle, the side reactions are severe in conventional Li-O<sub>2</sub> battery. Great difference in cathode morphology reveals the reason why the single-cathode Type B battery cannot completely discharge in the second cycle, but the double-cathode Type C battery can operate stably.



We also monitor the morphology of single-cathode and double-cathodes in Type B and C cells after 1, 100, 150, and 170 cycles. By SEM observations, it can be clearly seen that some of the products/by-products gradually accumulate on the inner and outer cathodes in Type B cell (Figure S16). In contrast, the surfaces of the inner and outer cathodes in Type C cell are clean (Figure S17). In addition, Raman spectra further confirm that the species on the inner and outer cathodes in Type B cell are  $\text{CH}_3\text{COOLi}$ ,  $\text{Li}_2\text{CO}_3$ , and undecomposed  $\text{Li}_2\text{O}_2$ . However, the corresponding substances cannot be detected on the electrode of Type C cell (Figures S18 and S19). This further proves that double-cathode structured batteries can inhibit side reactions by enabling the stable and effective electron transfer among cathode, RM catalysts, and  $\text{Li}_2\text{O}_2/\text{O}_2$  during cycling.

To verify the stable state of inner and outer electrodes after cycling, we removed and cleaned the inner and outer cathodes of Type B and C batteries after different cycle numbers (1, 100, 150, and 170) and reassembled the cell with RM catalysts (without  $\text{O}_2$ ). By analyzing the cyclic voltammetry curves of DBBQ redox molecules on electrodes, the electron transfer ability between the electrode and RM catalysts was verified. As shown in Figures 5H and 5I, when the numbers of cycles experienced by the cathodes of the Type B cell increase, its redox peak current values gradually decrease. This indicates that the products/by-products gradually accumulate on the surface of the inner and outer cathodes of the Type B cell as the cycles progress, resulting in a decrease in the electrochemically active area. In sharp contrast, the cyclic voltammetry peak current values from Type C cell remain constant, showing that the electrochemically active areas of the inner and outer cathodes in Type C cell are stable. No accumulation of products/by-products is found on the surface of the double cathodes in the Type C cell. This further proves the much-enhanced activation ability of the double-cathode structure for RM catalysts. DEMS analysis was further performed to clarify this point. The cathodes of Type B cell after 150 cycles show low voltage on discharge and high voltage on charge, indicating that the accumulated products from side reactions on the electrode surface affect the formation and decomposition of  $\text{Li}_2\text{O}_2$ . The ratios of  $2e^-/\text{O}_2$  during discharge and charge of Type B cell are 1.23 and 1.22, respectively, which are much greater than 1.00 (Figure S20). After 170 cycles in Type C cell, the overpotentials for  $\text{Li}_2\text{O}_2$  formation and decomposition reactions are still small, and the charge voltages are maintained at  $\sim 4.0$  V (Figure S21). The  $2e^-/\text{O}_2$  ratio of Type C (1.09 during discharge and 1.07 during charge) is much lower than those of Type B.

### Influence of $\text{O}_2$ membrane surface porosity on battery performance

According to the abovementioned results, the  $\text{O}_2$  membrane has a decisive effect on battery performance by decoupling  $\text{O}_2$  mass transport and electron transfer. To further study the mechanism of the  $\text{O}_2$  barrier layer on battery cycle stability, we investigate the influence of  $\text{O}_2$  membrane surface porosity on battery performance. To obtain barrier layers with different surface porosity, polypropylene film treated by Harrick plasma with different time.  $\text{O}_2$  barrier layer with different surface porosity (Figures 6A-6C) were assembled. As shown in Figure 6D, when the surface porosity are 80%, 50%, and 15% in Type C cells, the discharge capacities reach 10.5, 13.8, and 20.8  $\text{mAh cm}^{-2}$ , respectively, indicating that the cell capacity is highly related to  $\text{O}_2$  membrane surface porosity. Figure 6E shows the cycle stability of Type C cells containing an  $\text{O}_2$  barrier layer with different surface porosity. As the surface porosity of the  $\text{O}_2$  barrier layer decreases, the cycle life of the battery is substantially extended as well. To analyze the above process, we further used iodometric titrations to quantitatively analyze  $\text{Li}_2\text{O}_2$  deposits on the inner and outer cathodes of the Type C cell (Figure 6F). When the  $\text{O}_2$  membrane surface porosity is 80%, 50%, and 15%, the ratios of deposited  $\text{Li}_2\text{O}_2$  on the outer/inner cathode are 57%/43%, 66%/34%, and 81%/19%, respectively. Notably, when the surface porosity of the  $\text{O}_2$  barrier layer is only 15%, the quantity of  $\text{Li}_2\text{O}_2$  deposited in the inner cathode is the lowest (19%) with the longest cycle life (684 cycles compared to 171 cycles of the Type B battery). Obviously, using an  $\text{O}_2$  membrane with low surface porosity could ensure the maximum decoupling of  $\text{Li}_2\text{O}_2$  nucleation/storage and electron transfer, which is significant for extending the cycle life of cells.

Furthermore, we used COMSOL software to simulate  $\text{O}_2$  mass transport and the quantity of deposited  $\text{Li}_2\text{O}_2$  during the discharge process of Type C cells containing  $\text{O}_2$  membrane with different surface porosities. As the  $\text{O}_2$  membrane surface porosity decreases, the  $\text{O}_2$  concentration difference between the inner cathode and the outer cathode gradually increases, implying that the surface porosity of the  $\text{O}_2$  membrane can adjust the rate and level of  $\text{O}_2$  transport to the inner cathode (Figure S22). Correspondingly, from a simple  $\text{O}_2$  permeability experiment, as the surface porosity of the  $\text{O}_2$  membrane decreases, the transport rate and quantity of  $\text{O}_2$  from left to right can be significantly reduced. This also reflects changes in  $\text{O}_2$  barrier effects of membranes with different surface porosities on the inner cathode in Type C cell (Figure S11). Similarly, the diffusion simulation of DBBQLi and the permeability



experiment of DBBQ also illustrate the interrelationship between surface porosity and diffusion rate, which is consistent with O<sub>2</sub> barrier transport rate trends (Figures S12, S23 and S24). The simulated quantities of deposited Li<sub>2</sub>O<sub>2</sub> on the inner cathode also decrease as the surface porosities decrease, which matches the iodometric titration results (Figure S25). We then tested Type C cells with surface porosity of 80% and 50% by operating them for 170 cycles. A passivation film is observed on the electrode after cycling, and the thickness of the passivation film increases with increasing surface porosity (Figures 5, S26 and S27). This shows that surface porosity regulation for the O<sub>2</sub> barrier layer has a definite effect on ensuring the electron transfer ability of the inner cathode.

The above results confirm that a Li-O<sub>2</sub> battery with a double-cathode structure is significant for improving the battery capacity and cycle stability. O<sub>2</sub> membrane with low surface porosity can prevent O<sub>2</sub> transport to the inner cathode and protect the ability of the inner cathode to transfer electrons to activate RM catalysts. Then, the activated RM catalysts migrate to the outer cathode to promote the reaction rate and stability of Li<sub>2</sub>O<sub>2</sub> formation and decomposition. This new cell structure design ensures efficient activation of liquid RM catalysts and reduces charging potentials through new electron transfer channels. Therefore, undesired electron transfer is reduced, and cell cycle life is improved. To further verify the application of double-cathode structured Type C cell in a relatively practical processes, we tested them in air atmosphere with a humidity of 25%. As shown in Figure 6G, the cycle life of a lithium-air (Li-air) battery with a double-cathode structure reaches 486 cycles, which is 4 times that of Type B cell. This further confirms the key role of the double-cathode structure in Li-O<sub>2</sub> and Li-air batteries.

## DISCUSSION

In summary, to address short cycle life in Li-O<sub>2</sub> batteries due to non-conductive discharge products and severe side reactions, we propose that O<sub>2</sub> mass transport and cathodic electron transfer reactions could be decoupled at space scale in a double-cathode structured battery. This structure can continuously and effectively enable stable electron transfer among cathode, RM catalysts, and Li<sub>2</sub>O<sub>2</sub>/O<sub>2</sub>, solves the accumulation of products/by-products, and improves Li<sub>2</sub>O<sub>2</sub> reaction kinetics. As a result, double-cathode Li-O<sub>2</sub> batteries exhibit superior cycle life compared to that of single-cathode batteries. The current problems of double-cathode-structured Li-O<sub>2</sub> batteries mainly come from the degradation reaction of RM catalysts on the lithium anode, causing deactivation of the RM catalysts in the later stage of battery cycling. However, these issues can be resolved by developing efficient membrane materials. Therefore, we strongly believe that decoupling mass transport and electron transfer within double-cathode structures represents an important advancement in the fundamental development and practical application of these batteries. In future studies, this new cell design could provide important reference values for upgrading the operational stability of other metal-rechargeable batteries whose discharge products are non-conductive and insoluble.

## EXPERIMENTAL PROCEDURES

### Resource Availability

#### Lead Contact

Further information and requests for resources should be directed to and will be fulfilled by the Lead Contact, Yong Zhao ([zhaoyong@henu.edu.cn](mailto:zhaoyong@henu.edu.cn)).

#### Materials Availability

This study did not generate new unique reagents.

#### Data and Code Availability

The datasets generated in this study are available from the lead contact on reasonable request.

## Materials and Methods

### Materials preparation.

Anhydrous tetraethylene glycol dimethyl ether (TEGDME), diethylene glycol dimethyl ether (DME), and lithium bis(trifluoromethane)sulfonimide (LiTFSI) were purchased from Suzhou Dodochem Co. Ltd., China. The water content was below 20 ppm for solvents and 40 ppm for Li salts. 2,5-di-tert-butyl-1,4-benzoquinone (DBBQ) was purchased from Aladdin, China. 2,2,6,6-tetramethyl-1-piperidinyloxy (TEMPO) was purchased from Macklin, China. Carbon nano-membranes (CNM) were purchased from NanoTechLabs Inc. (NTL-12211), United States. Glass microfiber filters (GF) were purchased from Whatman. (GF/C, 1822), Britain. Polypropylene (PP) membranes were purchased from Celgard.(2500), United States. Carbon



nanotube (CNT) was obtained from Tianjin Aiweixin Co. Ltd., China. All materials for battery assembly were stored in an Ar-filled glovebox.

### Electrochemical cyclic voltammetry (CV)

CV tests of Lithium-Carbon (Li-C) cells were performed using Metrohm Autolab. The measurements were carried out at room temperature (25 °C) under argon atmosphere. Carbon electrodes were used as the working electrodes. Metallic lithium was employed as both reference and counter electrodes.

### Li-O<sub>2</sub> cells assembly

Li-O<sub>2</sub> batteries were assembled in an Ar-filled glove box. Outer cathode was prepared through conventional methods with powder CNT. In detail, 90 wt% of CNT, 10 wt% of polyvinylidene fluoride (PVDF) in methyl-2-pyrrolidone (NMP) were mixed homogeneously and then coated on the stainless steel substrate (1 cm<sup>2</sup>). Subsequently, the electrodes were heated at 110 °C for 10 h under vacuum. The loading mass of CNT was controlled at 0.45 ± 0.1 mg cm<sup>-2</sup>. The O<sub>2</sub> barrier layer was from the PP membrane treated by Harrick plasma (Model: PDC-32G-2). After plasma treatment for 0, 5, 10 minutes respectively, O<sub>2</sub> barrier layers with surface porosities of 15%, 50%, 80% can be obtained. The surface porosity and thickness of the O<sub>2</sub> barrier layer were measured and calculated by analysis of surface pore area with scanning electron microscope. The inner cathode was CNM with a diameter of 1.6 cm and the part outside the circle is 0.2 mm wide and 0.5 mm long. O<sub>2</sub> barrier layer was employed to separate the outer and inner cathode, and they were wetted with electrolyte containing RMs (30 μL). The electrolyte was prepared by mixing LiTFSI (1 M), DBBQ (0.05 M), TEMPO (0.2 M), and TEGDME in an Ar-filled glove box. During the cell assembly process, anode and cathode were separated by a PSS-Li/GO-Li/GF membrane and a glass fiber separator infiltrated with electrolyte containing RMs. To protect the lithium anode, PSS-Li/GO-Li/GF membrane is placed between the lithium anode and the glass fiber separator. The detailed procedure for synthesizing the PSS-Li/GO-Li/GF membrane has been described in our previous reports.<sup>52</sup> For the Li-O<sub>2</sub> with double-cathodes, the electrolyte was dropped into the glass fiber on the surface of PSS-Li/GO-Li/GF membrane by pipetting with a solution dosage of 60 μL. To keep the experimental conditions consistent, 90 μL of electrolyte containing RMs was dropped on the glass fiber in the Li-O<sub>2</sub> with single-cathode. All the batteries were tested at room temperature (30°C) with a potential range of 2.0-4.9 V. Li-O<sub>2</sub> batteries were measured at a gas mixture of O<sub>2</sub>/Ar (4/1, v/v) in a sealed chamber. Li-air batteries were measured at air-atmosphere with 25% of the humidity in realistic conditions. A gas pressure of 1 bar is applied in the Li-O<sub>2</sub> and Li-air batteries.

### Physical characterization.

To investigate discharge products on the cathodes, the batteries were disassembled in an Ar-filled glovebox and the cathodes were washed with glycol DME three times. Then, the electrode was dried for further characterization. The X-ray diffraction (XRD) test was conducted with a powder XRD system using Cu K $\alpha$  radiation (D8-ADVANCE, Bruker, Germany). Electrode morphology was observed by a field emission scanning electron microscope (Gemini500, Carl Zeiss, Germany). Raman spectra were measured with a Renishaw-in-Via spectrometer (10 mW, 532 nm).

### Chemical titration

The discharged cathodes were disassembled in an Ar glove box and cleaned with DME solvents. Then bases formed on the cathodes were titrated with a standard 0.05 M HCl solution (phenolphthalein was used as the end-point indicator). After finishing titration, three reagents were added to the existing solution in turn: 1 mL of 2 wt% KI in H<sub>2</sub>O, 1 mL of 3.5 M H<sub>2</sub>SO<sub>4</sub>, and 50 μL of a molybdate-based catalyst solution. The peroxide solution color turned to yellow upon adding reagent due to I<sub>2</sub> formation, and the I<sub>2</sub> is immediately titrated to a faint straw color using 0.05 M NaS<sub>2</sub>O<sub>3</sub>. At this point, ~0.5 mL of a 1% starch indicator was added to the solution, and the color turned dark blue. The titration was continuously operated until the solution turned transparent. The Li<sub>2</sub>O<sub>2</sub> yield is defined as the percentage of titrated peroxide quantities on the inner cathodes or outer cathodes to the total titration quantity. The Li<sub>2</sub>O<sub>2</sub> yield of outer cathodes is the sum of the outer cathode and O<sub>2</sub> barrier layer in the Li-O<sub>2</sub> batteries with double-cathodes. Detailed procedures for titration of Li<sub>2</sub>O<sub>2</sub> was described in previous reports.<sup>53</sup>

### UV-Vis analysis

UV-vis absorption spectra were measured with a UV-visible near infrared spectrophotometer (PE Lambda 950) with a wavelength range from 200 nm to 800 nm. TEGDME electrolytes containing 50 mM DBBQ were used as the original solution. After maintaining a static state



for 1 h and 12 h, the permeated solution in the right bottle was diluted with TEGDME (1:20). Then UV absorption spectra were performed.

### Differential electrochemical mass spectrometry

Differential electrochemical mass spectrometry (DEMS) system was built in-house based on a commercial quadrupole mass spectrometer (Hiden HPR-40) with a turbomolecular pump (Edwards EXT75DX). The DEMS cell had a customized Swagelok design with two PEEK capillary tubes as a purge gas inlet and outlet. The cell assembly was carried out in an Ar glovebox. For DEMS testing, a mixture gas of O<sub>2</sub>/Ar (4/1, v/v) with a flux of 0.5 mL min<sup>-1</sup> controlled by a digital flow meter (Bronkhorst) was used. During the discharge process, the cells were discharged at a current of 2 mA cm<sup>-2</sup> with a cut-off capacity of 2 mAh cm<sup>-2</sup>. During the charging process, pure Ar with a flux of 0.5 mL min<sup>-1</sup> was used as the carrier gas, and the cells were charged at a current of 1 mA cm<sup>-2</sup>.

### SUPPLEMENTAL INFORMATION

Document S1 is the main supplemental PDF:

Document S1. Supplemental Experimental Procedures, Figures S1–S25, Table S1–S3 and Note S1.

### ACKNOWLEDGMENTS

The authors gratefully acknowledge National Natural Science Foundation of China (21773055, 51702086, 21203055, 21805070). The authors thank Dr. Zuliang Du, Mr. Lin Zhang, Dr. Binbin Hu, Dr. Shilong Jiao, Danzheng Zhou, Qing Chen from Henan University for their valuable discussion. Work at Argonne National Laboratory was supported by the U. S. Department of Energy (DOE), Office of Energy Efficiency and Renewable Energy, Vehicle Technologies Office under Clean Vehicles, US-China Clean Energy Research Centre (CERC-CVC2). Argonne National Laboratory is operated for DOE Office of Science by Chicago Argonne, LLC, under contract number DE-AC02-06CH11357.

### AUTHOR CONTRIBUTIONS

Q. Han and Y. Zhao developed the concept. Q. Han and W. Guo designed the experiment. Q. Han, W. Guo, X. He, X. Liu, X. Zhu and T. Bian carried out the electrochemical and physical characterizations. Q. Han, T. Liu, Jun Lu, Y. Zhao and L. Jiang discussed the results and co-wrote the paper. All of the authors discussed the results and reviewed the manuscript.

### DECLARATION OF INTERESTS

The authors declare no competing interests.

### REFERENCES\*

1. Peng, Z., Freunberger, S.A., Chen, Y., and Bruce, P.G. (2012). A Reversible and Higher-Rate Li–O<sub>2</sub> Battery. *Science* *337*, 563–566. 10.1126/science.1223985.
2. Xia, C., Kwok, C.Y., and Nazar, L.F. (2018). A high-energy-density lithium-oxygen battery based on a reversible four-electron conversion to lithium oxide. *Science* *361*, 777. 10.1126/science.aas9343.
3. Lim, H.-D., Lee, B., Bae, Y., Park, H., Ko, Y., Kim, H., Kim, J., and Kang, K. (2017). Reaction chemistry in rechargeable Li–O<sub>2</sub> batteries. *Chem. Soc. Rev.* *46*, 2873–2888. 10.1039/C6CS00929H.
4. Lu, J., Li, L., Park, J.-B., Sun, Y.-K., Wu, F., and Amine, K. (2014). Aprotic and Aqueous Li–O<sub>2</sub> Batteries. *Chem. Rev.* *114*, 5611–5640. 10.1021/cr400573b.
5. Zhang, P., Zhao, Y., and Zhang, X. (2018). Functional and stability orientation synthesis of materials and structures in aprotic Li–O<sub>2</sub> batteries. *Chem. Soc. Rev.* *47*, 2921–3004. 10.1039/C8CS00009C.
6. Cong, G., Wang, W., Lai, N.-C., Liang, Z., and Lu, Y.-C. (2019). A high-rate and long-life organic–oxygen battery. *Nat. Mater.* *18*, 390–396. 10.1038/s41563-019-0286-7.
7. Asadi, M., Sayahpour, B., Abbasi, P., Ngo, A.T., Karis, K., Jokisaari, J.R., Liu, C., Narayanan, B., Gerard, M., Yasaei, P., et al. (2018). A lithium–oxygen battery with a long cycle life in an air-like atmosphere. *Nature* *555*, 502–506. 10.1038/nature25984.
8. Hartmann, P., Bender, C.L., Vračar, M., Dürr, A.K., Garsuch, A., Janek, J., and Adelhelm, P. (2013). A rechargeable room-temperature sodium superoxide (NaO<sub>2</sub>) battery. *Nat. Mater.* *12*, 228–232. 10.1038/nmat3486.
9. Gao, X., Chen, Y., Johnson, L.R., Jovanov, Z.P., and Bruce, P.G. (2017). A rechargeable lithium–oxygen battery with dual mediators stabilizing the carbon cathode. *Nat. Energy* *2*, 17118. 10.1038/nenergy.2017.118.
10. Aetukuri, N.B., McCloskey, B.D., García, J.M., Krupp, L.E., Viswanathan, V., and Luntz, A.C. (2015). Solvating additives drive solution-mediated electrochemistry

- and enhance toroid growth in non-aqueous Li–O<sub>2</sub> batteries. *Nat. Chem.* **7**, 50–56. 10.1038/nchem.2132.
- Mahne, N., Schafzahl, B., Leypold, C., Leypold, M., Grumm, S., Leitgeb, A., Strohmaier, Gernot A., Wilkening, M., Fontaine, O., Kramer, D., et al. (2017). Singlet oxygen generation as a major cause for parasitic reactions during cycling of aprotic lithium–oxygen batteries. *Nat. Energy* **2**, 17036. 10.1038/nenergy.2017.36.
  - Freunberger, S.A., Chen, Y., Drewett, N.E., Hardwick, L.J., Bardé, F., and Bruce, P.G. (2011). The Lithium–Oxygen Battery with Ether-Based Electrolytes. *Angew. Chem. Int. Ed.* **50**, 8609–8613. 10.1002/anie.201102357.
  - Freunberger, S.A., Chen, Y., Peng, Z., Griffin, J.M., Hardwick, L.J., Bardé, F., Novák, P., and Bruce, P.G. (2011). Reactions in the Rechargeable Lithium–O<sub>2</sub> Battery with Alkyl Carbonate Electrolytes. *J. Am. Chem. Soc.* **133**, 8040–8047. 10.1021/ja2021747.
  - Qiao, Y., Wu, S., Yi, J., Sun, Y., Guo, S., Yang, S., He, P., and Zhou, H. (2017). From O<sub>2</sub><sup>•−</sup> to HO<sub>2</sub><sup>•</sup>: Reducing By-Products and Overpotential in Li–O<sub>2</sub> Batteries by Water Addition. *Angew. Chem. Int. Ed.* **56**, 4960–4964. 10.1002/anie.201611122.
  - Adams, B.D., Black, R., Williams, Z., Fernandes, R., Cuisinier, M., Berg, E.J., Novak, P., Murphy, G.K., and Nazar, L.F. (2015). Towards a Stable Organic Electrolyte for the Lithium Oxygen Battery. *Adv. Energy. Mater.* **5**, 1400867. 10.1002/aenm.201400867.
  - Xiong, Q., Huang, G., and Zhang, X.-B. (2020). High-Capacity and Stable Li–O<sub>2</sub> Batteries Enabled by a Trifunctional Soluble Redox Mediator. *Angew. Chem. Int. Ed.* **59**, 19311–19319. 10.1002/anie.202009064.
  - Wandt, J., Jakes, P., Granwehr, J., Gasteiger, H.A., and Eichel, R.-A. (2016). Singlet Oxygen Formation during the Charging Process of an Aprotic Lithium–Oxygen Battery. *Angew. Chem. Int. Ed.* **55**, 6892–6895. 10.1002/anie.201602142.
  - Zhang, P., Ding, M., Li, X., Li, C., Li, Z., and Yin, L. (2020). Challenges and Strategy on Parasitic Reaction for High-Performance Nonaqueous Lithium–Oxygen Batteries. *Adv. Energy. Mater.* **10**, 2001789. 10.1002/aenm.202001789.
  - Shu, C., Wang, J., Long, J., Liu, H.-K., and Dou, S.-X. (2019). Understanding the Reaction Chemistry during Charging in Aprotic Lithium–Oxygen Batteries: Existing Problems and Solutions. *Adv. Mater.* **31**, 1804587. 10.1002/adma.201804587.
  - Kwak, W.-J., Kim, H., Petit, Y.K., Leypold, C., Nguyen, T.T., Mahne, N., Redfern, P., Curtiss, L.A., Jung, H.-G., Borisov, S.M., et al. (2019). Deactivation of redox mediators in lithium–oxygen batteries by singlet oxygen. *Nat. Commun.* **10**, 1380. 10.1038/s41467-019-09399-0.
  - Lin, X., Yuan, R., Cai, S., Jiang, Y., Lei, J., Liu, S.-G., Wu, Q.-H., Liao, H.-G., Zheng, M., and Dong, Q. (2018). An Open-Structured Matrix as Oxygen Cathode with High Catalytic Activity and Large Li<sub>2</sub>O<sub>2</sub> Accommodations for Lithium–Oxygen Batteries. *Adv. Energy. Mater.* **8**, 1800089. 10.1002/aenm.201800089.
  - Liu, T., Leskes, M., Yu, W., Moore, A.J., Zhou, L., Bayley, P.M., Kim, G., and Grey, C.P. (2015). Cycling Li–O<sub>2</sub> batteries via LiOH formation and decomposition. *Science* **350**, 530. 10.1126/science.aac7730.
  - Lu, J., Lei, Y., Lau, K.C., Luo, X., Du, P., Wen, J., Assary, R.S., Das, U., Miller, D.J., Elam, J.W., et al. (2013). A nanostructured cathode architecture for low charge overpotential in lithium–oxygen batteries. *Nat. Commun.* **4**, 2383. 10.1038/ncomms3383.
  - Jung, J., Dong Won, C., Lee, C., Yoon, K.R., Yu, S., Cheong, J., Kim, C., Cho, S.-H., Park, J.-S., Park, Y., and Kim, I.-D. (2018). Rational design of protective In<sub>2</sub>O<sub>3</sub> layer-coated carbon nanopaper membrane: Toward stable cathode for long-cycle Li–O<sub>2</sub> batteries. *Nano Energy* **46**, 193–202. 10.1016/j.nanoen.2018.01.045.
  - Wang, P., Ren, Y., Wang, R., Zhang, P., Ding, M., Li, C., Zhao, D., Qian, Z., Zhang, Z., Zhang, L., and Yin, L. (2020). Atomically dispersed cobalt catalyst anchored on nitrogen-doped carbon nanosheets for lithium–oxygen batteries. *Nat. Commun.* **11**, 1576. 10.1038/s41467-020-15416-4.
  - Xie, J., Yao, X., Madden, I.P., Jiang, D.-E., Chou, L.-Y., Tsung, C.-K., and Wang, D. (2014). Selective Deposition of Ru Nanoparticles on TiSi<sub>2</sub> Nanonet and Its Utilization for Li<sub>2</sub>O<sub>2</sub> Formation and Decomposition. *J. Am. Chem. Soc.* **136**, 8903–8906. 10.1021/ja504431k.
  - Oh, S.H., Black, R., Pomerantseva, E., Lee, J.-H., and Nazar, L.F. (2012). Synthesis of a metallic mesoporous pyrochlore as a catalyst for lithium–O<sub>2</sub> batteries. *Nat. Chem.* **4**, 1004–1010. 10.1038/nchem.1499.
  - Lai, J., Xing, Y., Chen, N., Li, L., Wu, F., and Chen, R. (2020). Electrolytes for Rechargeable Lithium–Air Batteries. *Angew. Chem. Int. Ed.* **59**, 2974–2997. 10.1002/anie.201903459.
  - Guo, Z., Li, C., Liu, J., Wang, Y., and Xia, Y. (2017). A Long-Life Lithium–Air Battery in Ambient Air with a Polymer Electrolyte Containing a Redox Mediator. *Angew. Chem. Int. Ed.* **56**, 7505–7509. 10.1002/anie.201701290.
  - Huang, Z., Zeng, H., Xie, M., Lin, X., Huang, Z., Shen, Y., and Huang, Y. (2019). A Stable Lithium–Oxygen Battery Electrolyte Based on Fully Methylated Cyclic Ether. *Angew. Chem. Int. Ed.* **58**, 2345–2349. 10.1002/anie.201812983.
  - Liu, Z., Huang, J., Zhang, Y., Tong, B., Guo, F., Wang, J., Shi, Y., Wen, R., Zhou, Z., Guo, L., and Peng, Z. (2019). Taming Interfacial Instability in Lithium–Oxygen Batteries: A Polymeric Ionic Liquid Electrolyte Solution. *Adv. Energy. Mater.* **9**, 1901967. 10.1002/aenm.201901967.
  - Tong, B., Huang, J., Zhou, Z., and Peng, Z. (2018). The Salt Matters: Enhanced Reversibility of Li–O<sub>2</sub> Batteries with a Li[(CF<sub>3</sub>SO<sub>2</sub>)(n-C<sub>4</sub>F<sub>9</sub>SO<sub>2</sub>)N]-Based Electrolyte. *Adv. Mater.* **30**, 1704841. 10.1002/adma.201704841.
  - Kondori, A., Jiang, Z., Esmaeilirad, M., Tamadoni Saray, M.,

- Kakekhani, A., Kucuk, K., Navarro Munoz Delgado, P., Maghsoudipour, S., Hayes, J., Johnson, C.S., et al. (2020). Kinetically Stable Oxide Overlayers on Mo<sub>3</sub>P Nanoparticles Enabling Lithium–Air Batteries with Low Overpotentials and Long Cycle Life. *Adv. Mater.* *32*, 2004028. 10.1002/adma.202004028.
34. Song, L.-N., Zhang, W., Wang, Y., Ge, X., Zou, L.-C., Wang, H.-F., Wang, X.-X., Liu, Q.-C., Li, F., and Xu, J.-J. (2020). Tuning lithium-peroxide formation and decomposition routes with single-atom catalysts for lithium–oxygen batteries. *Nat. Commun.* *11*, 2191. 10.1038/s41467-020-15712-z.
35. Zhang, P., Zhang, S., He, M., Lang, J., Ren, A., Xu, S., and Yan, X. (2017). Realizing the Embedded Growth of Large Li<sub>2</sub>O<sub>2</sub> Aggregations by Matching Different Metal Oxides for High-Capacity and High-Rate Lithium Oxygen Batteries. *Adv. Sci.* *4*, 1700172. 10.1002/advs.201700172.
36. Bhattacharya, P., Nasybulin, E.N., Engelhard, M.H., Kovarik, L., Bowden, M.E., Li, X.S., Gaspar, D.J., Xu, W., and Zhang, J.-G. (2014). Dendrimer-Encapsulated Ruthenium Oxide Nanoparticles as Catalysts in Lithium–Oxygen Batteries. *Adv. Funct. Mater.* *24*, 7510-7519. 10.1002/adfm.201402701.
37. Song, S., Xu, W., Zheng, J., Luo, L., Engelhard, M.H., Bowden, M.E., Liu, B., Wang, C.-M., and Zhang, J.-G. (2017). Complete Decomposition of Li<sub>2</sub>CO<sub>3</sub> in Li–O<sub>2</sub> Batteries Using Ir/B<sub>4</sub>C as Noncarbon-Based Oxygen Electrode. *Nano Lett.* *17*, 1417-1424. 10.1021/acs.nanolett.6b04371.
38. Hassoun, J., Croce, F., Armand, M., and Scrosati, B. (2011). Investigation of the O<sub>2</sub> Electrochemistry in a Polymer Electrolyte Solid-State Cell. *Angew. Chem. Int. Ed.* *50*, 2999-3002. 10.1002/anie.201006264.
39. Wong, R.A., Yang, C., Dutta, A., O, M., Hong, M., Thomas, M.L., Yamanaka, K., Ohta, T., Waki, K., and Byon, H.R. (2018). Critically Examining the Role of Nanocatalysts in Li–O<sub>2</sub> Batteries: Viability toward Suppression of Recharge Overpotential, Rechargeability, and Cyclability. *ACS Energy Lett.* *3*, 592-597. 10.1021/acsenergylett.8b00054.
40. Ko, Y., Park, H., Lee, K., Kim, S.J., Park, H., Bae, Y., Kim, J., Park, S.Y., Kwon, J.E., and Kang, K. (2020). Anchored Mediator Enabling Shuttle-Free Redox Mediation in Lithium–Oxygen Batteries. *Angew. Chem. Int. Ed.* *59*, 5376-5380. 10.1002/anie.201916682.
41. Gao, X., Chen, Y., Johnson, L., and Bruce, Peter G. (2016). Promoting solution phase discharge in Li–O<sub>2</sub> batteries containing weakly solvating electrolyte solutions. *Nat. Mater.* *15*, 882-888. 10.1038/nmat4629.
42. Zhang, Y., Wang, L., Zhang, X., Guo, L., Wang, Y., and Peng, Z. (2018). High-Capacity and High-Rate Discharging of a Coenzyme Q10-Catalyzed Li–O<sub>2</sub> Battery. *Adv. Mater.* *30*, 1705571. 10.1002/adma.201705571.
43. Zhang, P., Liu, L., He, X., Liu, X., Wang, H., He, J., and Zhao, Y. (2019). Promoting Surface-Mediated Oxygen Reduction Reaction of Solid Catalysts in Metal–O<sub>2</sub> Batteries by Capturing Superoxide Species. *J. Am. Chem. Soc.* *141*, 6263-6270. 10.1021/jacs.8b13568.
44. Sun, D., Shen, Y., Zhang, W., Yu, L., Yi, Z., Yin, W., Wang, D., Huang, Y., Wang, J., Wang, D., and Goodenough, J.B. (2014). A Solution-Phase Bifunctional Catalyst for Lithium–Oxygen Batteries. *J. Am. Chem. Soc.* *136*, 8941-8946. 10.1021/ja501877e.
45. Bergner, B.J., Schürmann, A., Pepler, K., Garsuch, A., and Janek, J. (2014). TEMPO: A Mobile Catalyst for Rechargeable Li–O<sub>2</sub> Batteries. *J. Am. Chem. Soc.* *136*, 15054-15064. 10.1021/ja508400m.
46. Wang, X.-G., Zhang, Z., Zhang, Q., Wang, C., Zhang, X., Xie, Z., and Zhou, Z. (2019). MoCl<sub>5</sub> as a dual-function redox mediator for Li–O<sub>2</sub> batteries. *J. Mater. Chem. A* *7*, 14239-14243. 10.1039/C9TA03628H.
47. Lim, H.-D., Lee, B., Zheng, Y., Hong, J., Kim, J., Gwon, H., Ko, Y., Lee, M., Cho, K., and Kang, K. (2016). Rational design of redox mediators for advanced Li–O<sub>2</sub> batteries. *Nat. Energy* *1*, 16066. 10.1038/nenergy.2016.66.
48. Jung, H.-G., Hassoun, J., Park, J.-B., Sun, Y.-K., and Scrosati, B. (2012). An improved high-performance lithium–air battery. *Nat. Chem.* *4*, 579-585. 10.1038/nchem.1376.
49. Liang, Z., Zhou, Y., and Lu, Y.-C. (2018). Dynamic oxygen shield eliminates cathode degradation in lithium–oxygen batteries. *Energy Environ. Sci.* *11*, 3500-3510. 10.1039/C8EE02067A.
50. Liu, X., Zhang, P., Liu, L., Feng, J., He, X., Song, X., Han, Q., Wang, H., Peng, Z., and Zhao, Y. (2020). Inhibition of Discharge Side Reactions by Promoting Solution-Mediated Oxygen Reduction Reaction with Stable Quinone in Li–O<sub>2</sub> Batteries. *ACS Appl. Mater. Inter.* *12*, 10607-10615. 10.1021/acscami.0c01105.
51. Mourad, E., Petit, Y.K., Spezia, R., Samojlov, A., Summa, F.F., Prehal, C., Leybold, C., Mahne, N., Slugovc, C., Fontaine, O., et al. (2019). Singlet oxygen from cation driven superoxide disproportionation and consequences for aprotic metal–O<sub>2</sub> batteries. *Energy Environ. Sci.* *12*, 2559-2568. 10.1039/C9EE01453E.
52. Liang, D., Bian, T., Han, Q., Wang, H., Song, X., Hu, B., He, J., and Zhao, Y. (2020). Inhibiting the shuttle effect using artificial membranes with high lithium-ion content for enhancing the stability of the lithium anode. *J. Mater. Chem. A* *8*, 14062-14070. 10.1039/C9TA13304F.
53. McCloskey, B.D., Valery, A., Luntz, A.C., Gowda, S.R., Wallraff, G.M., Garcia, J.M., Mori, T., and Krupp, L.E. (2013). Combining Accurate O<sub>2</sub> and Li<sub>2</sub>O<sub>2</sub> Assays to Separate Discharge and Charge Stability Limitations in Nonaqueous Li–O<sub>2</sub> Batteries. *J. Phys. Chem. Lett.* *4*, 2989-2993. 10.1021/jz401659f.

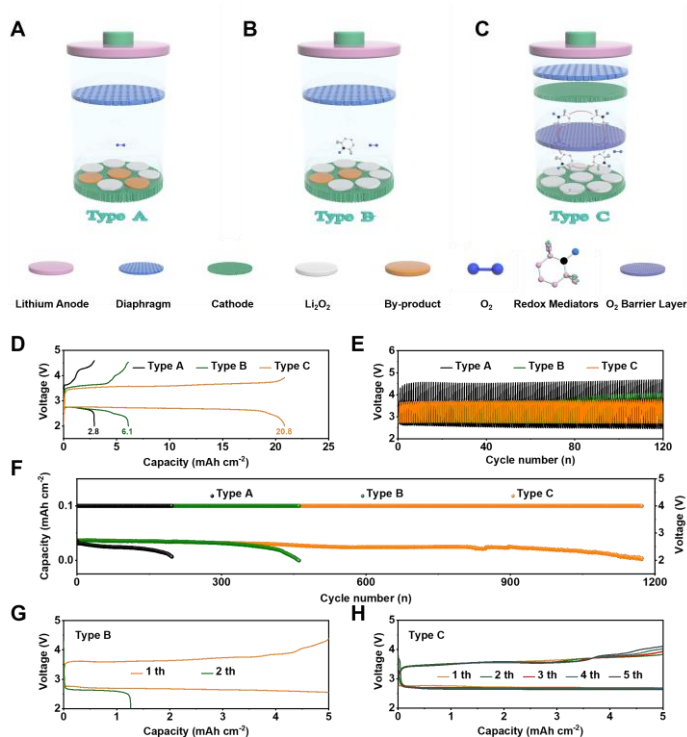


**Figure 1. Schematics and performance of the different types of Li-O<sub>2</sub> batteries**

(A) Conventional Li-O<sub>2</sub> battery without a RM catalyst (Type A). (B) Single-cathode Li-O<sub>2</sub> battery with RM catalysts (Type B). (C) Double-cathode Li-O<sub>2</sub> battery with RM catalysts (Type C). (D) Full discharge-charge curves for three types of Li-O<sub>2</sub> batteries at a current of 0.1 mA cm<sup>-2</sup>. (E) The corresponding cycle number and voltage for the three types of batteries at a current of 0.2 mA cm<sup>-2</sup> with a 0.1 mAh cm<sup>-2</sup> capacity cut-off. (F) Voltage versus cycle number on the discharge terminal of Type A (black), Type B (green), and Type C (orange) batteries at a current of 0.2 mA cm<sup>-2</sup> in a fixed-capacity mode (fixed capacity: 0.1 mAh cm<sup>-2</sup>). (G) Galvanostatic voltage profiles of the Type B and (H) Type C batteries with a cut-off capacity of 5 mAh cm<sup>-2</sup> at a current of 0.1 mA cm<sup>-2</sup>. All measurements were conducted with 1 M LiTFSI, 50 mM DBBQ and 200 mM TEMPO in TEGDME electrolyte solutions.

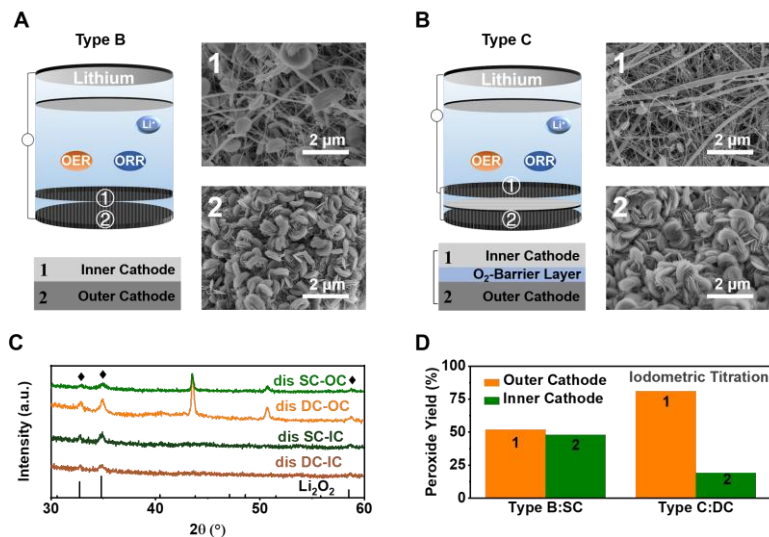


**Figure 2. Qualitative and quantitative analyses of discharge products**

Schematics and SEM images of the cathode of (A) Type B and (B) Type C batteries with a 5 mA h cm<sup>-2</sup> discharge capacity, where 1 refers to the inner cathode and 2 refers to the outer cathode (scale bar, 2 μm). (C) XRD pattern of the discharged cathodes in (A) and (B). SC-OC and SC-IC refer to the outer cathode and inner cathode respectively in single-cathode Type B battery; DC-OC and DC-IC refer to the outer cathode and inner cathode respectively in double-cathode Type C battery. (D) Li<sub>2</sub>O<sub>2</sub> deposition quantities obtained from iodometric titration performed on discharged outer (orange) and inner (green) cathodes with a limited capacity of 5 mA h cm<sup>-2</sup>, wherein the yield is defined as the percentage of the titrated peroxide quantity on the inner cathodes or outer cathodes to the total titration quantity. The Li<sub>2</sub>O<sub>2</sub> yield of the outer cathodes is the sum of the outer cathode and O<sub>2</sub> barrier layer for the double-cathode Li-O<sub>2</sub> battery.

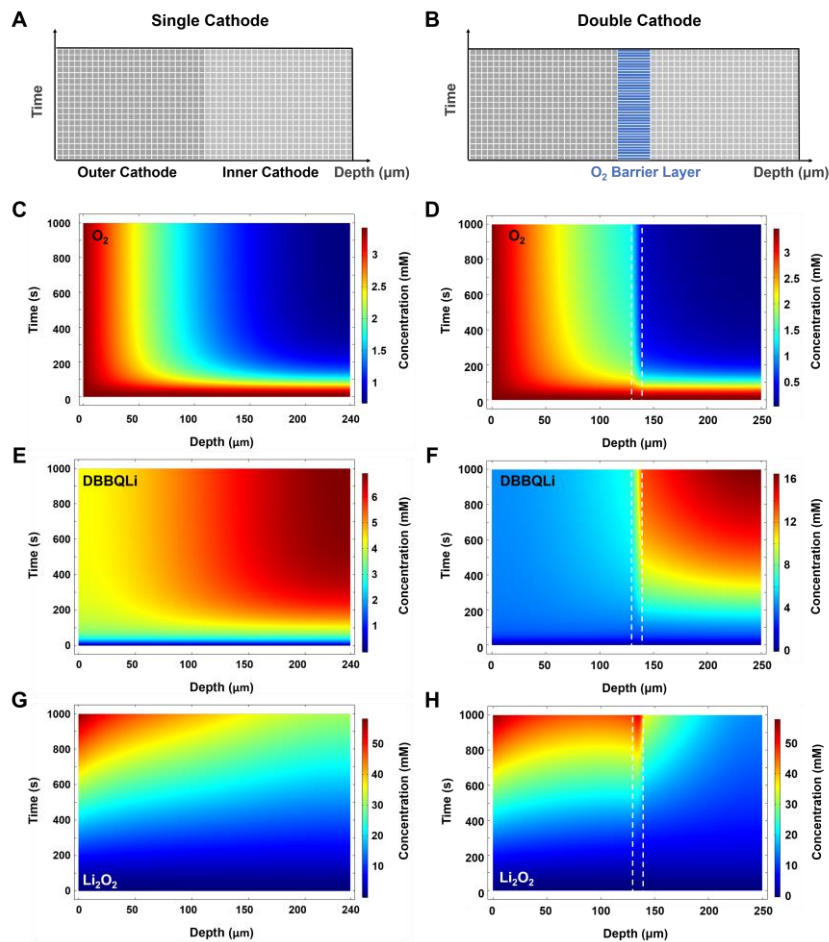


**Figure 3. Modelling and simulation study of the discharge process on the cathode side with COMSOL software**

Schematics of the cathode structure used for the modelling study of (A) a single cathode and (B) double cathodes in Type B and C batteries. (C to H) Simulated profiles of O<sub>2</sub>, DBBQLi, and Li<sub>2</sub>O<sub>2</sub> quantities (concentrations) in Li-O<sub>2</sub> batteries during discharge at 0.2 mA cm<sup>-2</sup> to 1000 seconds. (C) O<sub>2</sub>, (E) DBBQLi, and (G) Li<sub>2</sub>O<sub>2</sub> quantities of single cathodes in Type B batteries, and (D) O<sub>2</sub>, (F) DBBQLi, and (H) Li<sub>2</sub>O<sub>2</sub> quantities of double cathodes in Type C batteries. A depth of 0-130 μm represents the outer cathode, and a depth of 130-240 μm represents the inner cathode for the single-cathode battery. A depth of 0-130 μm represents the outer cathode, 130-140 μm represents the O<sub>2</sub> barrier layer, and 140-250 μm represents the inner cathode for the double-cathode battery. The pressure of the gas diffusion layer of Type B and C batteries is 1 bar.

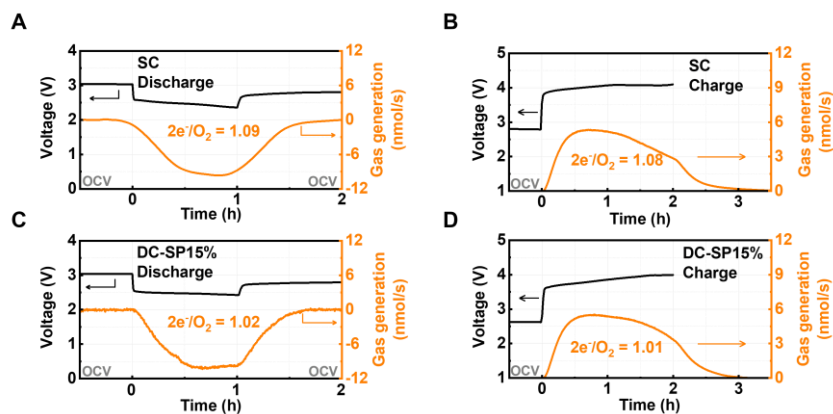


**Figure 4. The  $O_2$  consumption/evolution profiles measured by DEMS in single-cathode and double-cathode  $Li-O_2$  batteries**

(A to D) DEMS analysis of the  $Li-O_2$  battery. (A and B) Type B battery. (C and D) Type C battery.  $O_2$  consumption (A and C) during discharge at  $2\text{ mA cm}^{-2}$  and  $O_2$  evolution (B and D) during charge at  $1\text{ mA cm}^{-2}$  in a fixed-capacity mode (fixed capacity:  $2\text{ mAh cm}^{-2}$ ). OCV refers to open circuit voltage; SC refers to the single-cathode Type B battery; SP refers to the surface porosity of  $O_2$  barrier layer; DC-SP15% refers to the double-cathode Type C battery with SP15%  $O_2$  barrier layer.

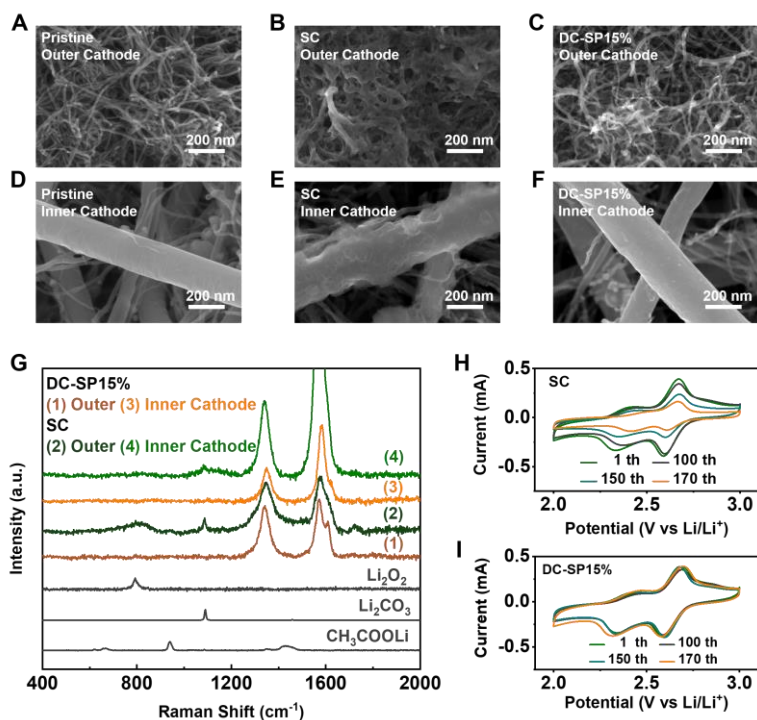


**Figure 5. Morphological composition and electrochemical analysis**

(A to F) SEM images of the outer and inner cathodes (scale bar, 200 nm). Pristine (A) outer and (D) inner cathodes. (B and E) The cathodes in a Type B battery with a single cathode and (C and F) those in a Type C battery with double cathodes after 170 cycles at a current of  $0.2 \text{ mA cm}^{-2}$  in fixed-capacity mode (fixed capacity:  $0.2 \text{ mAh cm}^{-2}$ ). (G) Raman spectroscopy of the outer and inner cathodes after 170 cycles in (B, C, E and F). (H and I) CV curves of 10 mM DBBQ within 1 M LiTFSI/TEGDME in a Li-C battery at  $2 \text{ mV s}^{-1}$  under an argon atmosphere. The positive electrodes come from the cathodes of (H) Type B and (I) C batteries after 1 (green), 100 (dark grey), 150 (dark cyan), and 170 (orange) cycles at a current of  $0.2 \text{ mA cm}^{-2}$  in fixed-capacity mode (fixed capacity:  $0.2 \text{ mAh cm}^{-2}$ ). SC refers to the single-cathode Type B battery; SP refers to the surface porosity of O<sub>2</sub> barrier layer; DC-SP15% refers to the double-cathode Type C battery with SP15% O<sub>2</sub> barrier layer.

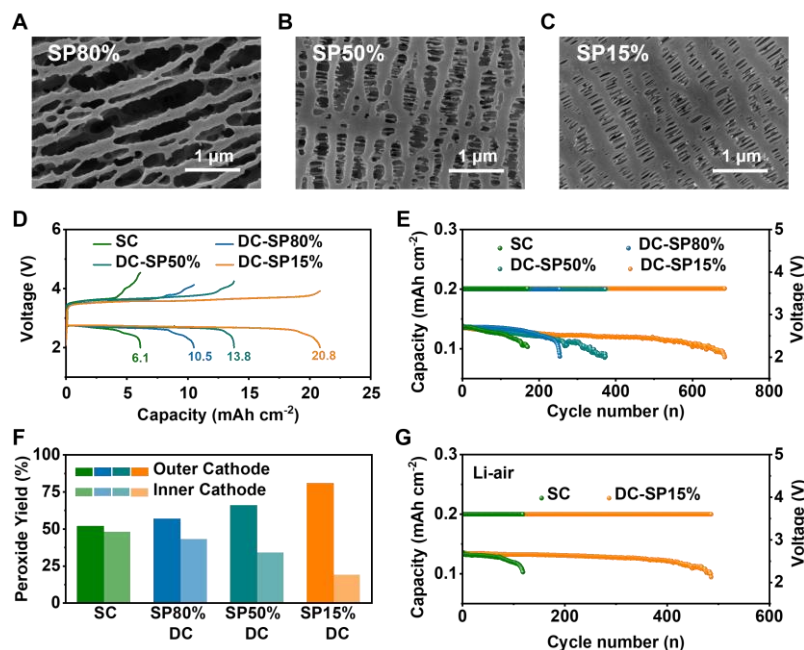
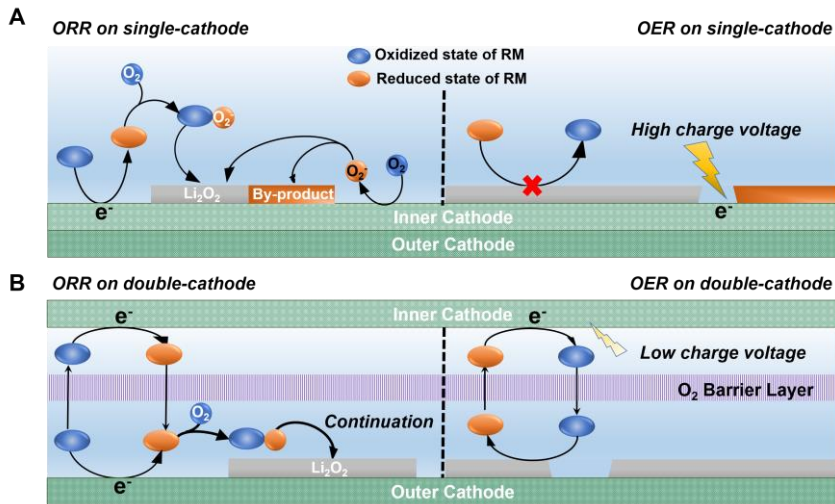


**Figure 6. Morphology of O<sub>2</sub> barrier layers with different surface porosities and their effect on battery stability**

(A to C) SEM images of O<sub>2</sub> barrier layers with different surface porosities (scale bar, 1 μm). Surface porosity (SP) values of (A) 80%, (B) 50% and (C) 15%. (D) Full discharge-charge curves of single-cathode Type B batteries (green) and double-cathode Type C batteries with SPs of 80% (blue), 50% (dark cyan), and 15% (orange) at 0.1 mA cm<sup>-2</sup> current. SC and DC refer to the single-cathode Type B battery and the double-cathode Type C battery respectively. (E) Voltage versus cycle number on the discharge terminal of Type B and C batteries at a current of 0.2 mA cm<sup>-2</sup> in a fixed-capacity mode (fixed capacity: 0.2 mAh cm<sup>-2</sup>). (F) Li<sub>2</sub>O<sub>2</sub> quantities obtained from iodometric titration experiments performed on the discharged outer (dark colours) and inner (light colours) cathodes, wherein the yield is defined as the percentage of the titrated peroxide quantity on the inner or outer cathodes to the total titration quantity. (G) Voltage versus cycle number on the discharge terminal of the single-cathode (green) and double-cathode (orange) Li-air batteries with an air humidity of 25% at 0.2 mA cm<sup>-2</sup> of current in fixed-capacity mode (fixed capacity: 0.2 mAh cm<sup>-2</sup>).



**Scheme 1. Schematics of the working mechanism in single-cathode and double-cathode Li-O<sub>2</sub> batteries**

Type B battery with a single cathode (A) during discharge (left) and charge (right). Type C battery with a double cathode (B) during discharge (left) and charge (right). ORR and OER refers to oxygen reduction reaction and oxygen evolution reaction respectively. RM refers to redox mediator.